

A zeolite family with expanding structural complexity and embedded isorecticular structures

Peng Guo^{1,#}, Jiho Shin^{2,#}, Alex G. Greenaway³, Jung Gi Min², Jie Su¹, Hyun June Choi², Leifeng Liu¹, Paul A. Cox⁴, Suk Bong Hong^{2,*}, Paul A. Wright^{3,*}, Xiaodong Zou^{1,*}

¹ Inorganic and Structural Chemistry and Berzelii Centre EXSELENT on Porous Materials, Department of Materials and Environmental Chemistry, Stockholm University, SE-106 91 Stockholm, Sweden.

² Centre for Ordered Nanoporous Materials Synthesis, School of Environmental Science and Engineering, POSTECH, Pohang 790-784, Korea.

³ EaStCHEM School of Chemistry, University of St. Andrews, St. Andrews, KY16 9ST, UK.

⁴ School of Pharmacy and Biomedical Sciences, University of Portsmouth, Portsmouth, PO1 2DT, UK.

These authors contributed equally to this work.

The prediction and synthesis of novel crystal structures makes possible the targeted preparation of materials with desired properties. Amongst porous solids, this has been achieved for metal-organic frameworks (MOFs)¹⁻³ but not for the more widely-applicable zeolites^{4,5}, where exploratory synthesis is the usual route to materials discovery. Although millions of hypothetical zeolite structures have been proposed^{6,7}, not enough is known about their synthesis mechanism to allow any given structure to be prepared. Here we present an approach that combines structure solution with structure prediction, and inspires subsequent synthesis of novel super-complex zeolites. We used electron diffraction to identify a family of related structures and discover the structural “coding” within them. This enabled us to determine the complex structure of the zeolite ZSM-25⁸, which has the largest unit cell of all known zeolites (91,554 Å³) and demonstrates highly selective CO₂ adsorption. Extension of the method enabled us to predict the other members of a family of increasingly complex but structurally-related zeolites and this inspired synthesis of two more complex zeolites, PST-20 and PST-25, with much larger cell volumes (166,988 and 275,178 Å³, respectively) and similar selective adsorption properties. Members of this family have the same symmetry but a continually expanding unit cell and are related by hitherto unseen structural principles; we call them *embedded isoreticular zeolite structures*.

The synthesis of novel porous materials with designed structures and properties has been realised for MOFs¹, where inorganic and organic building units of defined geometry assemble to give frameworks with predictable topology and functionality^{2,3}. This degree of control is difficult to achieve for purely inorganic frameworks^{4,5}. Geometrically-related structures have been prepared, for example using enlarged clusters^{9,10} or extended inorganic chains as building units¹¹, but the former requires major changes in framework chemistry and synthesis conditions and the latter uses organic templates that cannot be removed without structural collapse. For the most industrially-important class of microporous materials, zeolites, which have fully-connected frameworks of corner-sharing AlO₄ and SiO₄ tetrahedra, there are no examples where novel structures have been designed and then directly prepared. Millions of energetically-feasible hypothetical zeolite ‘structures’ have been predicted^{6,7}, but routes to their synthesis remain elusive.

Even when new zeolites are prepared, through exploratory synthesis, their structure solution takes time because they crystallise as powders. Nevertheless, complex zeolite structures can be solved, usually with help from the electron microscope¹². In one approach, powder X-ray diffraction (PXRD) intensity data is combined with structure factor phase information obtained from high-resolution electron microscopy (HRTEM) images¹³⁻¹⁶; in another, rotation electron diffraction (RED)^{17,18} has been applied to submicron-sized crystals¹⁹⁻²¹. Here, we used electron diffraction to solve a complex, long-unknown zeolite structure related to paulingite and discovered their common structural ‘coding’ via the ‘strong reflections’ method²². We extended this to predict a family of highly complex zeolite frameworks with unit cell volumes in excess of any previously reported - and then prepared two of them via rational synthesis.

ZSM-25, first reported in 1981⁸, was synthesised according to the literature using Na⁺ and tetraethylammonium (TEA⁺) ions as structure-directing agents (SDAs) (Methods)²³ as part of our search for selective adsorbents. It showed attractive CO₂ adsorption properties (described below), but its structure was not known. We therefore applied the RED method to ZSM-25 (NaTEA-ZSM-25) microcrystals (Fig. 1a,b, Methods, Extended Data Fig. 2a-c). The 3D RED data revealed that ZSM-25 is body-centred cubic ($a = 42.3 \text{ \AA}$) with Laue symmetry $m-3m$. However, electron beam damage causes low data resolution and prevents structure solution using direct methods. The IZA Database of Zeolite Structures²⁴ lists three frameworks with the same Laue symmetry as ZSM-25: **KFI** (ZK-5), **RHO** (Rho) and **PAU** (paulingite) all have the same space group $Im-3m$. Further, we found that the strong reflections of ZSM-25

are distributed in the same regions of reciprocal space as those calculated from **RHO** and **PAU** (Fig. 1a-d, Extended Data Fig. 3), indicating the **RHO**, **PAU** and ZSM-25 structures are related. Strong reflections represent the main structure features of a crystal and can be used for structure solution²⁵. We therefore thought that it might be possible to phase the strong reflections of ZSM-25 from the known **PAU** structure, and thus solve its structure. The twenty-one strongest symmetry-independent reflections were identified, and their phases assigned to be those calculated from corresponding reflections of the **PAU** structure (Fig. 1c,d, Extended Data Table 1). All 16 symmetry-independent T-atoms (T = Si, Al) were located from the 3D electron density map using the 21 reflections: oxygen atoms were placed between the T-atoms according to TO₄ tetrahedral geometry. The structure of as-made NaTEA-ZSM-25, including its aluminosilicate framework and extra-framework cation and water positions, was refined against synchrotron PXRD data (Fig. 2a, Methods).

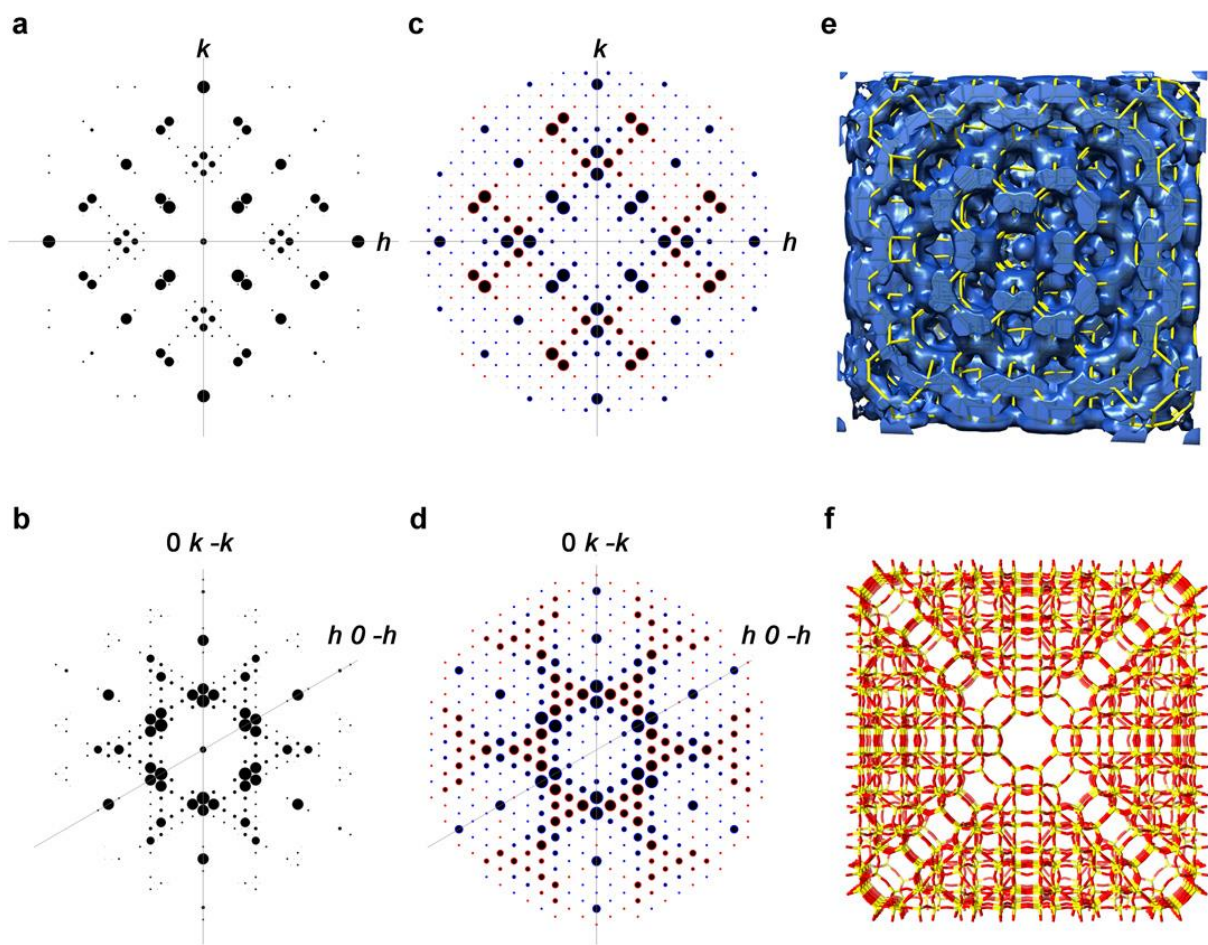


Figure 1 | Structure determination of ZSM-25 by the strong reflections approach. a,b, The 2D slice of $(h k 0)$ (**a**) and $(h k -h-k)$ (**b**) cut from the reconstructed 3D reciprocal lattice from the RED data. The symmetry $m-3m$ has been imposed for a better comparison. **c,d,** Simulated $(h k 0)$ (**c**) and $(h k -h-k)$ (**d**) diffraction patterns of the idealised **PAU** structure, with the structure factor phases marked in blue (180°) and red (0°). **e,** 3D map generated by using amplitudes obtained from RED of ZSM-25 and phases calculated from the structure of **PAU**. **f,** The framework structure of ZSM-25.

The ZSM-25 framework can be considered an expanded version of **PAU**. Both are built of seven different cage types²⁴, $[4^{12}6^88^6]$ (*lta*), $[4^88^2]$ (*d8r*), $[4^{12}8^6]$ (*pau*), $[4^66^28^6]$ (*t-plg*), $[4^58^3]$ (*t-oto*), $[4^68^4]$ (*t-gsm*) and $[4^78^5]$ (*t-phi*) (Fig. 2b). The maximum ring size in each is eight, establishing them as small pore zeolites. The *lta* cages are connected via chains of alternating *d8r* and *pau* cages along unit cell edges to form cubic scaffolds (Fig. 2c,d). The scaffold of ZSM-25 is extended from that of **PAU** by adding an extra pair of *pau* and *d8r* cages along each unit cell edge, expanding a by ~ 10 Å. In accordance with the body-centering, each

structure contains two such cubic scaffolds, interpenetrated. The space between the scaffolds is filled by the four other types of cages to form fully four-connected frameworks (Fig. 2e,f). All cages are inter-connected via 8-ring windows. The structure of **RHO** can be obtained by removing two pairs of *pau* and *d8r* cages on each unit cell edge, leaving only one *d8r* cage between the *lta* cages (Extended Data Fig. 6). **RHO**, **PAU** and ZSM-25 belong to the same family. **PAU** and ZSM-25 can be considered expanded versions of **RHO**. We call this the RHO-family, and denote Rho to be the 1st generation (RHO-G1), paulingite the 3rd (RHO-G3) and ZSM-25 the 4th (RHO-G4). It is interesting to predict the structure of other family members. While the structure of RHO-G2 with two *d8r* and one *pau* cages per unit cell edge ($a \approx 25 \text{ \AA}$) was generated previously^{26,27}, it is much more challenging to predict larger structures by modelling how the large space between the cubic scaffolds should be filled.

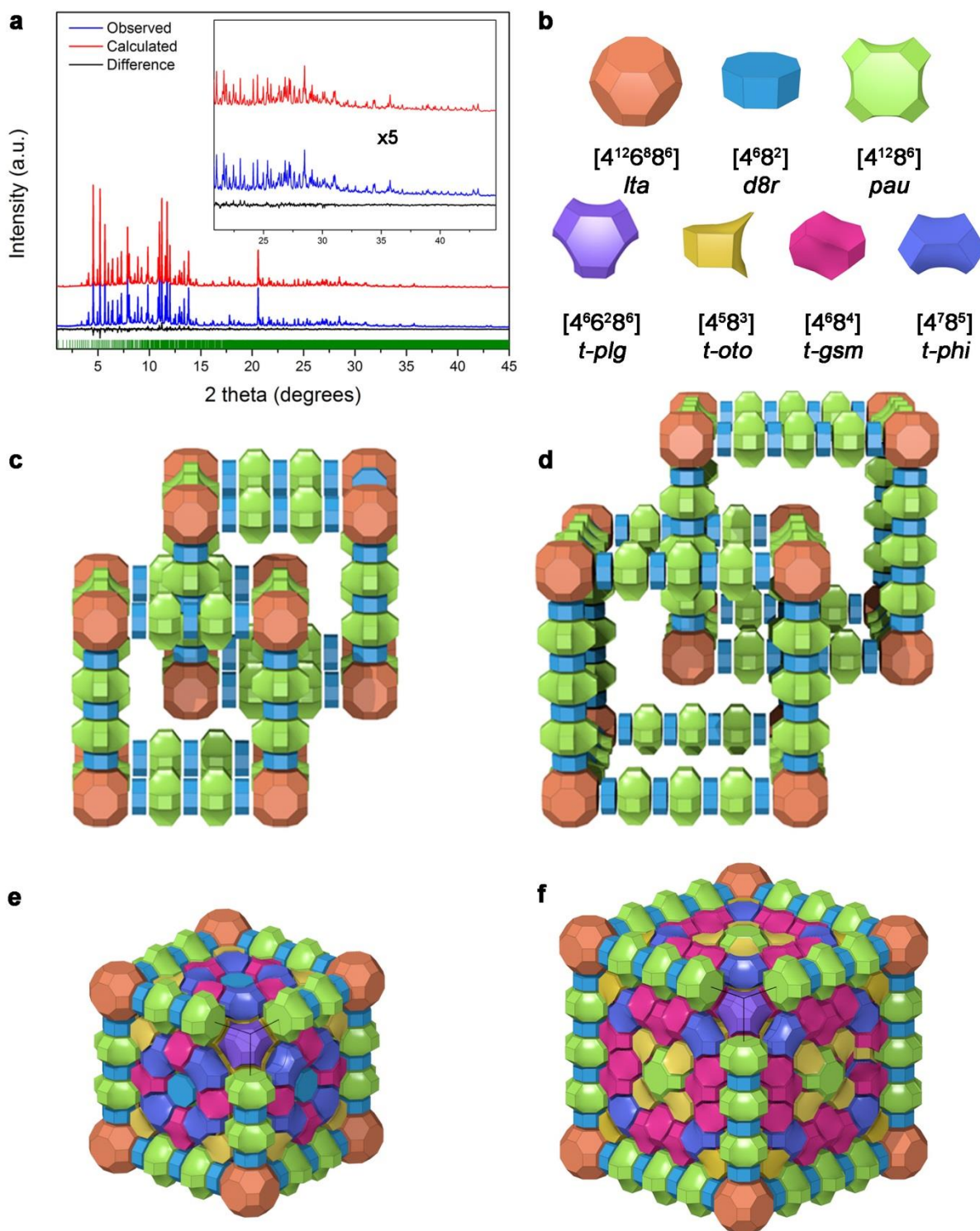


Figure 2 | PXRD profiles and structure description of ZSM-25. **a**, Rietveld refinement of as-made NaTEA-ZSM-25 ($\lambda = 0.63248 \text{ \AA}$). **b**, The seven different cages, $[4^{12}6^88^6]$ (*lta*), $[4^88^2]$ (*d8r*), $[4^{12}8^6]$ (*pau*), $[4^66^28^6]$ (*t-plg*), $[4^58^3]$ (*t-oto*), $[4^68^4]$ (*t-gsm*), and $[4^78^5]$ (*t-phi*) found in ZSM-25, as solid tiles. **c,d**, The connectivity of the *lta*, *d8r*, and *pau* cages in **PAU** (**c**) and ZSM-25 (**d**), showing the interpenetration of the two cubic scaffolds. The sequence is *lta-d8r-pau-d8r-pau-d8r-lta* for **PAU** and *lta-d8r-pau-d8r-pau-d8r-pau-d8r-lta* for ZSM-25. **e,f**, The

3D framework structure of **PAU** (e) and ZSM-25 (f) with *t-plg*, *t-oto*, *t-gsm*, and *t-phi* cages embedded in the scaffolds.

We anticipated that the structure relationship (structural “coding”) of the higher members of the RHO-family would also be reflected in reciprocal space, and that this could be exploited for structure prediction. We found that the structure factors of the strong reflections for ZSM-25 and **PAU** are indeed very similar (Fig. 3a, Extended Data Fig. 3). The framework of ZSM-25 could be predicted solely from the related **PAU** framework, without using any experimental diffraction data from ZSM-25 (Methods). We applied the same approach to predict the structures of other members; RHO-G2 from **PAU** (RHO-G3), RHO-G5 from ZSM-25 (RHO-G4), and RHO-G6 from RHO-G5 (Fig. 3b,c, Methods, Extended Data Fig. 5). The final energies per SiO₂ as a function of framework density for RHO-G1-G6 are consistent with the trends observed for known structures (Supplementary Fig. 2, Supplementary Table 12), indicating they are all energetically feasible. In principle, the number of members in the RHO-family is endless. New zeolites with expanding unit cell and complexity are achieved by adding new pairs of *d8r* and *pau* cages, and their structures can be predicted using a similar approach.

Except for RHO-G1 and RHO-G2, all other members comprise the same seven cages (Fig. 3c, Extended Data Fig. 6, Supplementary Tables 13, 14) and every T-atom is part of three 4-rings. We think that these common motifs arise as a consequence of a dominating aluminosilicate crystallisation pathway. That both ECR-18 (**PAU**) and ZSM-25 were synthesised using TEA⁺ and Na⁺ as SDAs, together with K⁺ in the case of ECR-18, led us to speculate that the larger members (e.g., RHO-G5 and RHO-G6) of this family could also be synthesised using these SDAs, in concert with other inorganic cations. Examination of the evolution of the numbers of different cages in the RHO-family showed that the numbers of *t-oto*, *t-gsm*, and *t-phi* cages grow much faster than those of the other four cage types (Supplementary Table 13). Furthermore, we were aware that the natural zeolites gismondine (**GIS**) and phillipsite (**PHI**), which contain *t-gsm* cages only (**GIS**) and *t-oto* and *t-phi* cages (**PHI**) as building units, possess significant amounts of alkaline-earth metal cations such as Ca²⁺ and even Ba²⁺ as extra-framework cations²⁴. This prompted us to introduce small amounts of different alkaline-earth cations to the ZSM-25 synthesis mixture to promote the preferential formation of *t-oto*, *t-gsm*, and *t-phi* cages and thus to favour crystallisation of the more complex members of the RHO-family.

Following the strategy described above, we were able to synthesise the hypothetical RHO-G5 phase, denoted PST-20 (Methods, Extended Data Fig. 1b, Supplementary Tables 1, 2). Its successful synthesis was confirmed by RED (Extended Data Fig. 2d-f) and Rietveld refinement (Extended Data Fig. 4). It is worth noting that while the crystallisation of PST-20 was sensitive to synthesis temperature and time, the presence of the alkaline-earth cations Ca^{2+} and particularly Sr^{2+} is required to direct its crystallisation. A pure sample of PST-20 was successfully prepared by addition of Sr^{2+} to the synthesis gel. Subsequent structural analysis revealed that the Sr^{2+} cations are located mainly within the 8-rings of its *t-oto*, *t-gsm*, and *t-phi* cages (Supplementary Fig. 6), validating our approach. Following the same rational approach, modification of the synthesis conditions by the addition of both Sr^{2+} and Ca^{2+} to the ‘ZSM-25’ gel before heating resulted in clear evidence that RHO-G6, the next, even more complex zeolite in the RHO-family has already been crystallised (Supplementary Fig. 9, Supplementary Table 3). Further work is in progress to obtain the pure form of this material, which we denote PST-25.

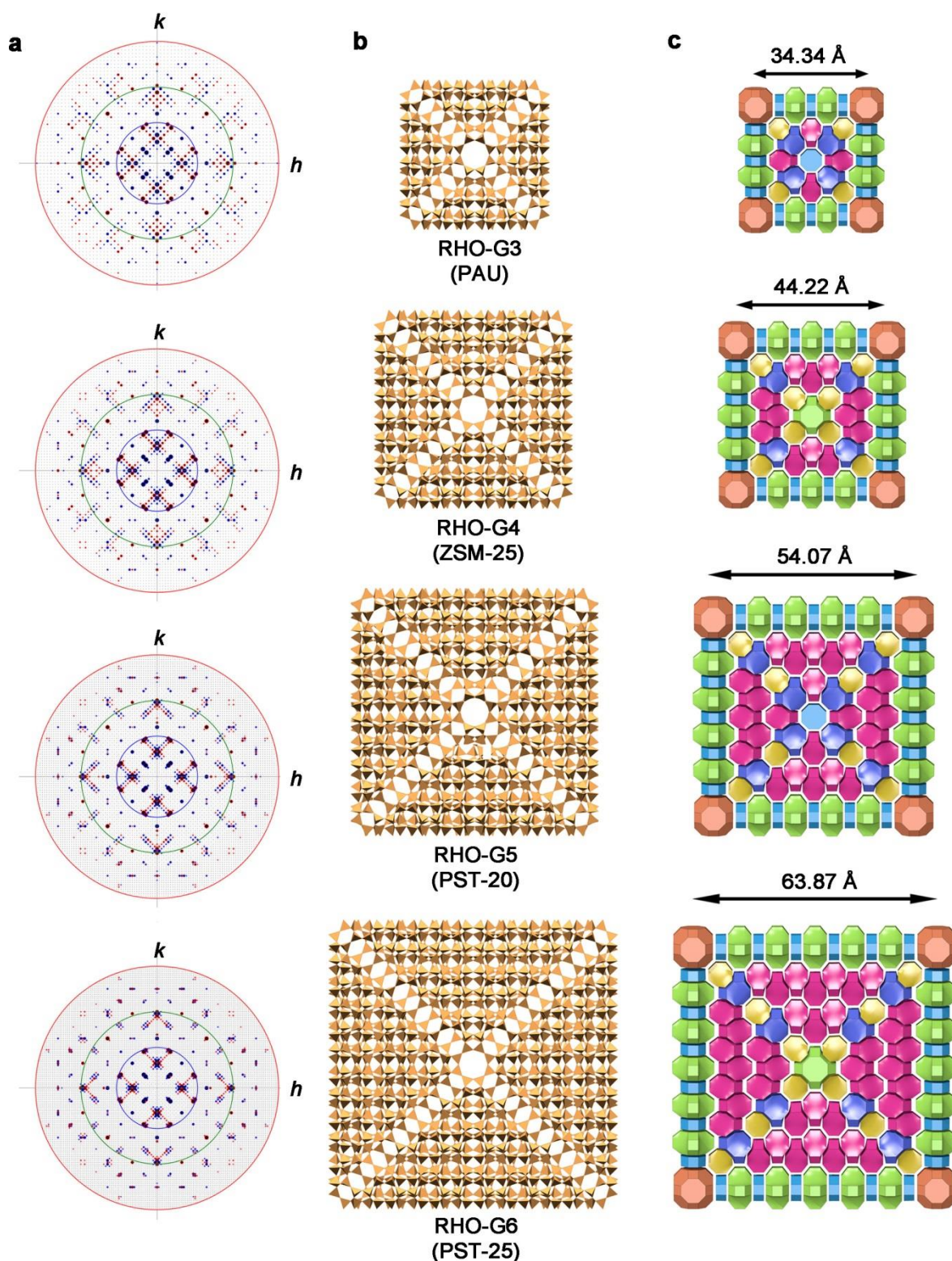


Figure 3 | Comparison of the reflection distributions and framework structures of RHO-G3-G6. **a**, The $(hk0)$ reciprocal plane showing the similar amplitude and phase distribution of the strong reflections. Reflections in red have phases 0° , while those in blue have phases 180° . The red, green, and blue circles correspond to 1.0, 1.6 and 3.0\AA d -spacing. **b,c**, Polyhedral (**b**) and tiling (**c**) representation of cross-sections (about 12\AA thick). The crystals corresponding to

RHO-G3-G6 have been synthesised as ECR-18, ZSM-25, PST-20, and PST-25, respectively. Note that the arrangement in the centre alternates every second structure in (c), i.e. is the similar for RHO-G3 and RHO-G5.

As with all members of this family, ZSM-25 and PST-20 (and PST-25) are accessible to molecules that can pass through 8-rings, and so the zeolites are potentially useful as small molecule adsorbents. Removal of CO₂ from natural gas or from flue gases²⁸ is one area of current interest for small pore zeolites. We found that NaTEA-ZSM-25 and Na⁺-exchanged NaSrTEA-PST-20 (denoted NaTEA-PST-20) show similarly high uptakes of CO₂ and low uptakes of N₂ and CH₄ (Fig. 4, Methods, Extended Data Table 2). The CO₂/CH₄ selectivity for all members of the RHO-family is high, and much greater than exhibited by the K-chabazite examined (Extended Data Table 2). We attribute this to the effect of cation gating, where cations blocking 8-ring windows in the structures are able to move to allow the passage of gas molecules that strongly interact with them, such as CO₂, but remain in place in the presence of weakly interacting molecules^{29,30}. Moreover, the CO₂ uptakes remained the same over 100 adsorption-desorption cycles (insets in Fig. 4a,b). The CO₂ uptake at 1.0 bar and 298 K was 3.5 mmol·g⁻¹ for NaTEA-ZSM-25 and 3.2 mmol·g⁻¹ for NaTEA-PST-20. These CO₂ uptakes are somewhat lower than that of Na-Rho (4.5 mmol·g⁻¹ at 1.0 bar and 298 K) but they are comparable with those observed for other well-studied small-pore zeolites such as K-chabazite (**CHA**, 3.6 mmol·g⁻¹). More significantly, while CO₂ adsorption on Na-Rho reached equilibrium only after *ca.* 2 h, uptake on NaTEA-ECR-18 was faster (equilibrating in 5 min) and NaTEA-ZSM-25 and NaTEA-PST-20 achieved equilibrium more quickly still (after *ca.* 2 min) (Figure 4c). Given their selective adsorption, fast kinetics and long-term stability, NaTEA-ZSM-25 and NaTEA-PST-20 are of potential interest as CO₂ adsorbents.

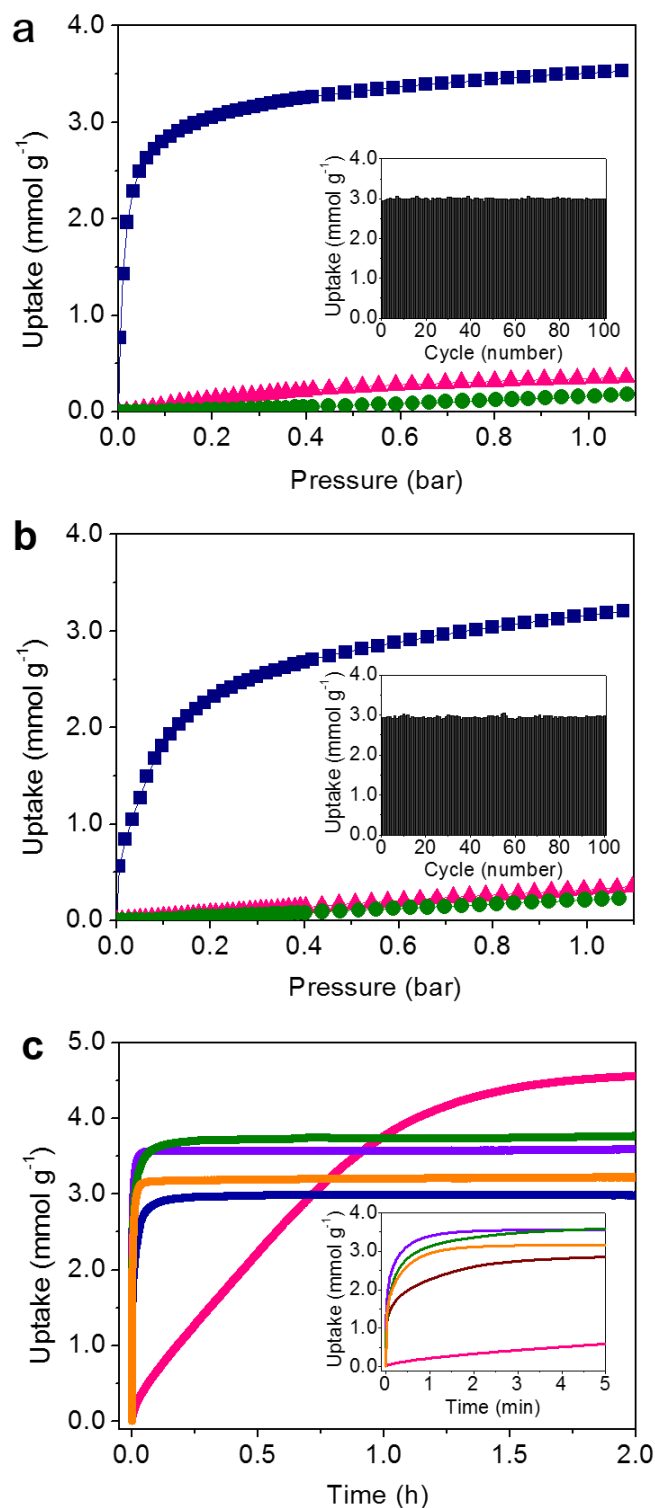


Figure 4 | Gas adsorption properties of NaTEA-ZSM-25 and NaTEA-PST-20. a, b, Adsorption isotherms at 298 K of CO₂ (navy), CH₄ (green), and N₂ (pink) for NaTEA-ZSM-25 (a) and NaTEA-PST-20 (b). Inset: CO₂ adsorption-desorption cycles at 343 K. c, CO₂ adsorption kinetics at 298 K and 1.2 bar on NaTEA-ZSM-25 (violet), NaTEA-PST-20 (orange), NaTEA-ECR-18 (navy), Na-Rho (pink), and K-chabazite (green).

Finally, structure expansion in the RHO-family operates at two levels (Fig. 3c, Extended Data Fig. 6, Supplementary Figs. 4c, 5c). First, the two-fold interpenetrated scaffold is expanded by inserting *pau* and *d8r* cages along each unit cell edge. Second, the space between the scaffolds is filled by four other cage types to form rigid, fully four-connected frameworks. The former expansion is isorecticular, as seen in MOFs¹⁻³, while the latter occurs by embedding four different cages in the inter-scaffold space. We call frameworks resulting from this principle of structure expansion ‘*embedded isorecticular*’; the RHO-family is the first example. While other families of expanded structures have the same topology and enlarged pore sizes^{2,3,11} (Supplementary Fig. 4a,b), the RHO-family members have different topologies but similar pore size (Supplementary Fig. 5b,c, Supplementary Tables 10, 11). The structural relationships among the RHO-family members become clear in reciprocal space, through the similar amplitude and phase distribution of reflections. This structural “coding” is useful both for structure solution and for prediction of new family members. It has inspired the syntheses of new zeolites with huge unit cells from chemically relatively simple systems - ZSM-25, PST-20, and PST-25 are the largest zeolites by unit cell volume - and it suggests a route to the rational synthesis of certain classes of zeolites.

References

1. Yaghi, O. M. *et al.* Reticular synthesis and the design of new materials. *Nature* **423**, 705-714 (2003).
2. Eddaoudi, M. *et al.* Systematic design of pore size and functionality in isorecticular MOFs and their application in methane storage. *Science* **295**, 469-472 (2002).
3. Deng, H. *et al.* Large-pore apertures in a series of metal-organic frameworks. *Science* **336**, 1018-1023 (2012).
4. Davis, M. E. Ordered porous materials for emerging applications. *Nature* **417**, 813-821 (2002).
5. Wang, Z., Yu, J. & Xu, R. Needs and trends in rational synthesis of zeolitic materials. *Chem. Soc. Rev.* **41**, 1729-1741 (2012).
6. Foster, M. D. & Treacy, M. M. J. Atlas of Prospective Zeolite Structures. <http://www.hypotheticalzeolites.net/>.
7. Deem, M. W. Deem Database. <http://www.hypotheticalzeolites.net/DATABASE/DEEM/index.php>.
8. Doherty, H. G., Plank, C. J. & Rosinski, E. J. Crystalline zeolite ZSM-25. US Patent 4,247,416 (1981).

9. Férey, G. Building units design and scale chemistry. *J. Solid State Chem.* **152**, 37-48 (2000).
10. Zou, X. D., Conradsson, T., Klingstedt, M., Dadachov, M. S. & O'Keeffe, M. A mesoporous germanium oxide with crystalline pore walls and its chiral derivative. *Nature* **437**, 716-719 (2005).
11. Lin, H.-Y. *et al.* Crystalline inorganic frameworks with 56-ring, 64-ring, and 72-ring channels. *Science* **339**, 811-813 (2013).
12. Willhammar, T., Yun, Y. F. & Zou, X. D. Structure determination: structural determination of ordered porous solids by electron crystallography. *Adv. Funct. Mater.* **24**, 173 (2014).
13. Zou, X. D., Hovmöller, S. & Oleynikov, P. *Electron Crystallography: electron microscopy and electron diffraction* (Oxford University Press, 2011).
14. Gramm, F. *et al.* Complex zeolite structure solved by combining powder diffraction and electron microscopy. *Nature* **444**, 79-81 (2006).
15. Baerlocher, C. *et al.* Structure of the polycrystalline zeolite catalyst IM-5 solved by enhanced charge flipping. *Science* **315**, 1113-1116 (2007).
16. Baerlocher, C. *et al.* Ordered silicon vacancies in the framework structure of the zeolite catalyst SSZ-74. *Nature Mater.* **7**, 631-635 (2008).
17. Zhang, D. L., Oleynikov, P., Hovmöller, S. & Zou, X. D. Collecting 3D electron diffraction data by the rotation method. *Z. Kristallogr.* **225**, 94-102 (2010).
18. Wan, W., Sun, J. L., Su, J., Hovmoller, S. & Zou, X. D. Three-dimensional rotation electron diffraction: software RED for automated data collection and data processing. *J. Appl. Crystallogr.* **46**, 1863-1873 (2013).
19. Willhammar, T. *et al.* Structure and catalytic properties of the most complex intergrown zeolite ITQ-39 determined by electron crystallography. *Nature Chem.* **4**, 188-194 (2012).
20. Martínez-Franco, R. *et al.* Synthesis of an extra-large molecular sieve using proton sponges as organic structure-directing agents. *Proc. Natl. Acad. Sci.* **110**, 3749-3754 (2013).
21. Hua, W. *et al.* A germanosilicate structure with 11×11×12-ring channels solved by electron crystallography. *Angew. Chem. Int. Ed.* **53**, 5868-5871 (2014).
22. Zhang, H., Zou, X. D., Oleynikov, P. & Hovmöller, S. Structure relations in real and reciprocal space of hexagonal phases related to i-ZnMgRE quasicrystals. *Philos. Mag.* **86**, 543-548 (2006).

23. Hong, S. B. *et al.* Synthesis and characterization of zeolite ZSM-25. *Stud. Surf. Sci. Catal.* **135**, 186-193 (2001).
24. Baerlocher, Ch. & McCusker, L. B. Database of Zeolite Structures. <http://www.iza-structure.org/databases/>.
25. Karle, J. & Karle, I. L. The symbolic addition procedure for phase determination for centrosymmetric and non-centrosymmetric crystals. *Acta Crystallogr.* **21**, 849-859 (1966).
26. Vaughan, D. E. W. & Strohmaier, K. G. Synthesis of ECR-18-a synthetic analog of paulingite. *Microporous Mesoporous Mater.* **28**, 233-239 (1999).
27. Blatov, V. A., Ilyushin, G. D., Lapshin, A. E. & Golubeva, O. Yu. Structure and chemical composition of the new zeolite ISC-1 from the data of nanocluster modeling. *Glass Phys. Chem.* **36**, 663-672 (2010).
28. Rochelle, G. T. Amine scrubbing for CO₂ capture. *Science* **325**, 1652-1654 (2009).
29. Shang, J. *et al.* Discriminative separation of gases by a “molecular trapdoor” mechanism in chabazite zeolites. *J. Am. Chem. Soc.* **134**, 19246-19253 (2012).
30. Lozinska, M. M. *et al.* Cation gating and relocation during the highly selective “trapdoor” adsorption of CO₂ on univalent cation forms of zeolite Rho. *Chem. Mater.* **26**, 2052-2061 (2014).

Supplementary Information is linked to the online version of the paper at www.nature.com/nature.

Acknowledgments: We acknowledge financial support from the Swedish Research Council (VR), the Swedish Governmental Agency for Innovation Systems (VINNOVA), the Röntgen-Ångström Cluster through the project grant MATsynCELL, the Knut & Alice Wallenberg Foundation through the project grant 3DEM-NATUR, the NCRI (2012R1A3A-2048833) and BK 21-plus programs through the National Research Foundation of Korea, and from the UK EPSRC (EP/J02077X/1). We acknowledge the ESRF, Grenoble (ID31, Prof. A.N. Fitch; ID22, Dr. C. Drathen) and the PAL, Pohang (9B, Dr. D. Ahn) for synchrotron X-ray beam times. We thank Prof. L.B. McCusker and Dr. C. Baerlocher for valuable suggestions about the Rietveld refinement. The TEM was financed by the Knut & Alice Wallenberg Foundation.

Author Contributions: S.B.H. and P.A.W. identified and initiated the research project, which was developed and brought to a conclusion jointly by S.B.H., P.A.W. and X.D.Z. J.S., J.G.M., H.J.C. and S.B.H. carried out the zeolite synthesis and gas sorption work. P.G.

conducted the TEM work. P.G., L.F.L. and X.D.Z. carried out the structure solution and structure prediction work. P.G., A.G.G., J.S., P.A.W. and X.D.Z. made the Rietveld refinements. P.A.C. did the molecular modelling and energy calculations. P.G., J.S., S.B.H., P.A.W. and X.D.Z. wrote and corrected the manuscript.

Author Information The Crystallography Information Files (CIFs) are deposited at the Cambridge Crystallographic Data Centre (<http://www.ccdc.cam.ac.uk>); CCDC numbers: 1031577 for as-made NaTEA-ZSM-25, 1057085 for calcined NaTEA-ZSM-25, 1057832 for as-made NaSrTEA-PST-20 and 1039878 for Na⁺-exchanged NaSrTEA-PST-20. Reprints and permissions information is available at npg.nature.com/reprintsandpermissions. The authors declare no competing financial interests. Correspondence and requests for materials should be addressed to S.B.H. (sbhong@postech.ac.kr), P.A.W (paw2@st-andrews.ac.uk) or X.D.Z. (xzou@mmk.su.se).

METHODS

Zeolite Syntheses. ZSM-25 was synthesised from aluminosilicate gels with a very narrow range of SiO₂/Al₂O₃ and Na₂O/SiO₂ ratios in the presence of TEABr, as reported by several groups^{8,23,31}. In a typical synthesis of ZSM-25, 1.92 g of Al(OH)₃•1.0H₂O were first mixed with a solution of 3.04 g of NaOH solution (50%, Aldrich) in 60.73 g of distilled water. To the resulting clear solution, 10.80 g of Ludox AS-40 (DuPont) and 11.15 g of TEABr (98%, Aldrich) were added. The resulting gel composition was 1.9Na₂O•1.0Al₂O₃•5.2TEABr•7.2SiO₂•390H₂O. The final synthesis mixture was stirred at room temperature for one day, charged into Teflon-lined 23-ml autoclaves and heated at 408 K under rotation (60 rpm) for 7 days.

PST-20 was synthesised using the organic SDA, TEA⁺, together with two inorganic SDAs Na⁺ and Sr²⁺ cations. In a typical synthesis of PST-20, 1.92 g of Al(OH)₃•1.0H₂O were first mixed with a solution of 3.04 g of 50% NaOH solution in 60.73 g of distilled water. To the resulting clear solution, 10.80 g of Ludox AS-40, 1.07 g of Sr(NO₃)₂ (Aldrich) and 11.15g of TEABr were added. The resulting gel composition was 1.9Na₂O•0.5SrO•1.0Al₂O₃•5.2TEABr•7.2SiO₂•390H₂O. If required, seed crystals (2wt% of anhydrous raw materials) were added to this gel. The seed crystals used here were PST-20 zeolite containing a small amount of ZSM-25 (<20%, according to PXRD analysis), which was previously prepared at 418 K for 4 days. The final synthesis mixture was stirred at room

temperature for one day, charged into Teflon-lined 23-ml autoclave, and heated at 418 K under rotation (60 rpm) for 2 days. Further details of PST-20 synthesis are given in Supplementary Table 1 and 2.

The solid products were recovered by filtration, washed repeatedly with water, and then dried overnight at room temperature. As-made ZSM-25 and PST-20 samples were characterised by PXRD, and ^{27}Al and ^{29}Si solid-state MAS NMR (Extended Data Fig. 1). The samples were calcined at 773 K in air for 8 h. PXRD patterns show that ZSM-25 retained its crystallinity but PST-20 lost crystallinity upon calcination. As-made PST-20 (NaSrTEA-PST-20) was refluxed twice in 1.0 M NaNO_3 solution at 353 K for 6 h (2.0g solid per 100 mL solution) to ensure that it was in its $\text{Na}^+\text{-TEA}^+$ form (denoted NaTEA-PST-20). For comparison, ECR-18 (**PAU**), zeolite Rho (**RHO**), and chabazite (**CHA**) with similar Si/Al ratios were also synthesised according to the procedures reported in the literature^{26,32,33} and converted to their Na^+ or K^+ forms.

Collection of rotation electron diffraction (RED) data. For RED data collection, powders of as-made NaTEA-ZSM-25 and NaSrTEA-PST-20 samples were dispersed in absolute ethanol and treated by ultrasonic treatment for 2 min. A droplet of the suspension was transferred onto a carbon-coated copper grid and dried in air. The 3D RED data were collected on a JEOL JEM2100 TEM at 200 kV using the *RED-data collection software*¹⁸. A single-tilt tomography sample holder was used for the data collection. The ED frames were recorded on a 12-bit Gatan ES500W Erlangshen camera side-mounted at a 35 mm port. For NaTEA-ZSM-25, the tilt step was 0.10° and the exposure time was 3.0s per ED frame. The tilt range was 76.71° and the total data collection time was about 70 min. Because NaSrTEA-PST-20 was more electron beam sensitive than NaTEA-ZSM-25, shorter data collection time (17 min) was used, with a larger tilt step (0.20°), shorter exposure time (1.0 s per ED frame) and a tilt range of 49.98° (Supplementary Table 4).

The data processing was performed using the *software RED-data processing*¹⁸. The unit cell was determined from the positions of the diffraction spots detected in the ED frames. The RED data show that both NaTEA-ZSM-25 and NaSrTEA-PST-20 are body-centred cubic with the Laue symmetry of $m\bar{3}m$ (Extended Data Fig. 2). The unit cell parameter determined from the RED data was $a=42.3 \text{ \AA}$ for NaTEA-ZSM-25 and $a=52.4 \text{ \AA}$ for NaTEA-ZSM-25 (Supplementary Table 4). The reflection conditions were deduced from the reconstructed reciprocal lattice to be $hkl: h+k+l=2n$, $hk0: h+k=2n$, $hkh: k=2n$, $00l: l=2n$. From the Laue symmetry and reflection conditions, the possible space

groups are $I432$ (No. 211), $I-43m$ (No. 217), and $Im-3m$ (No. 229). The intensity for each reflection was extracted from the ED frame with the highest intensity value. The final list of reflections with the indices and intensity was output to an HKL file for SHELX³⁴.

Structure determination of ZSM-25. Three zeolite frameworks were identified that have the same Laue group as ZSM-25: ZK-5 (KFI, $a=18.75$ Å), zeolite Rho (**RHO**, $a=15.03$ Å) and paulingite³⁵ (**PAU**, $a=35.09$ Å). The crystallographic structure factors were calculated from the atomic coordinates of the idealised framework given in the Database of Zeolite Structures²⁴. It was found that the strong reflections of ZSM-25 are distributed in the same locations in reciprocal space as those calculated from **PAU** (Fig. 2a-d). Twenty-one symmetry-independent reflections up to 2.5 Å resolution with amplitudes larger than 30% of the strongest reflection were identified from the RED data, and their phases were assigned to be those of structure factor phases calculated from corresponding reflections of the **PAU** structure (Fig. 2c,d, Extended Data Table 1). The indices of the required corresponding reflections in the **PAU** structure were obtained by scaling according to the unit cells: $h_{\text{PAU}}=h_{\text{ZSM-25}}\times a_{\text{PAU}}/a_{\text{ZSM-25}}$, $k_{\text{PAU}}=k_{\text{ZSM-25}}\times a_{\text{PAU}}/a_{\text{ZSM-25}}$, $l_{\text{PAU}}=l_{\text{ZSM-25}}\times a_{\text{PAU}}/a_{\text{ZSM-25}}$ (Extended Data Table 1). The 3D electron density map was calculated by inverse Fourier transformation from the amplitudes and phases of these strong reflections using the SUPERFLIP software (Fig. 2e)³⁶. All 16 symmetry-independent T-atoms (T=Si,Al) were located from the 3D electron density map using the software EDMA³⁷. The oxygen atoms were placed between the T-atoms according to SiO₄ tetrahedral geometry. The final model is a four-connected 3D framework (Fig. 2f), which was geometrically optimised using TOPAS Academic 4.1³⁸. Every T-atom is part of three 4-rings (in two different chains of 4-rings), accounting for the characteristic IR and Raman spectra reported previously for ZSM-25²³.

Rietveld refinement (ZSM-25 and PST-20) and profile fitting (PST-25). High-resolution PXRD data of as-made NaTEA-ZSM-25 was collected at room temperature at experimental station ID31 at the ESRF, Grenoble ($\lambda=0.632480$ Å). PXRD data of calcined NaTEA-ZSM-25 (Extended Data Fig. 1a) was obtained in flat plate mode using a PANalytical X'Pert PRO diffractometer ($\lambda=1.5418$ Å). High-resolution PXRD data of as-made and Na⁺-exchanged NaSrTEA-PST-20 were collected at 100 K at experimental station ID22 at the ESRF, Grenoble ($\lambda=0.40091$ Å). The samples were sealed in glass capillaries of 0.7 mm in diameter. Rietveld refinement was performed using TOPAS Academic V4.1³⁸. High-resolution PXRD data of a sample with a mixture of PST-25 and PST-20 (Run 18, Supplementary Table 3) was collected in flat plate mode on the 9B beamline at the Pohang Acceleration Laboratory, Korea

($\lambda=1.4640$ Å). Profile fitting was performed in the 2θ range of $10\text{--}70^\circ$ by the LeBail method³⁹ using the GSAS suite of programs⁴⁰.

For NaTEA-ZSM-25, the background was fitted with a 16th order Chebychev polynomial. The refinement was conducted using a PearsonVII peak profile function, followed by refinement of unit cell ($a=45.0711(3)$ Å) and zero-shift. The chemical formula was deduced from EDS, TGA and CHN analyses to be $[(\text{N}(\text{C}_2\text{H}_5)_4)_{40}\text{Na}_{285}(\text{H}_2\text{O})_{600}][\text{Si}_{1115}\text{Al}_{325}\text{O}_{2880}]$. The organic TEA⁺ cations were suggested by molecular modelling to be located in the *pau* and *t-plg* cages (Supplementary Fig. 1 and Supplementary Table 5), and Na⁺ and water molecule positions were arrived at by comparison with the structure of as-made paulingite³⁵ and by difference Fourier analysis. Considering the ratio of Si/Al=3.4, soft restraints were placed on the T-O distances (1.64 Å, T=Si,Al) and O...O distances (2.68 Å) within the TO₄ tetrahedra. All T positions were refined with the same and fixed occupancies. Additional Na⁺ cations and guest water molecules were located from the difference Fourier maps by fixing the framework of ZSM-25. All atomic positions were refined in the final cycles. The Debye-Waller factors of T, O, C and N atoms were fixed to 0.8, 1, 10 and 10, respectively, while those of Na⁺ and water molecules were refined. The final refinement converged to $R_{wp}=0.0537$, $R_p=0.0414$ and $GOF=2.87$ (Fig. 3a, Supplementary Table 6).

There are 16 T-atoms, 40 oxygen atoms, four TEA⁺ and 13 Na⁺, and 24 water molecules in the asymmetric unit of NaTEA-ZSM-25. Most Na⁺ cations are located in the 8-rings of the *t-oto*, *d8r* and *t-gsm* cages, some of them are partially occupied and sometimes share the same positions with guest water molecules. A Na⁺ cation (Na12, occupancy of 0.51) is found at the 6-ring connecting the *lta* and *t-plg* cages. There are about 296 Na⁺ cations in one unit cell, which is consistent with the chemical analysis. The TEA⁺ cations are disordered in the *pau* and *t-plg* cages. The final refinement shows that there is one TEA⁺ in each *pau* cage, and 0.85 and 0.80 TEA⁺ in *t-plg* cages (there are two symmetry-independent *t-plg* cages), respectively. The *t-plg* cages contain both TEA⁺ cations and guest water molecules, with a total occupancy of 1.0. The final framework structure has reasonable T-O bond distances (1.64 ± 0.02 Å) and O-T-O angles ($109.3^\circ\pm 4.5^\circ$) and T-O-T angles ($132\text{--}159^\circ$).

Rietveld refinement of the calcined, hydrated ZSM-25 was carried out in a similar way to that of NaTEA-ZSM-25, with the obvious difference that no TEA⁺ cations remain in the solid ($a=44.9242(16)$ Å, Supplementary Fig. 7 and Supplementary Table 7).

For as-made NaSrTEA-PST-20, the unit cell formula derived by elemental analysis and structure refinement was $[(\text{N}(\text{C}_2\text{H}_5)_4)_{56}\text{Na}_{162}\text{Sr}_{210}(\text{H}_2\text{O})_{563}][\text{Al}_{638}\text{Si}_{2002}\text{O}_{5280}]$. The starting structure was based on the model of RHO-G5 established during the prediction of larger structures of the RHO-family. The background was fitted with a 30th order Chebychev polynomial. The refinement was conducted using a TCHZ peak profile function, followed by refinement of unit cell ($a=55.0437(16)$ Å) and zero-shift. Soft restraints were placed on the T-O distances (1.64 Å, T=Si,Al) and O...O distances (2.68 Å) within the TO_4 tetrahedra. All T positions were refined with the same and fixed occupancies. The location of TEA^+ cations was modelled using the positions obtained from the structural model of NaTEA-ZSM-25, where TEA^+ cations were in the *pau* and *t-plg* cages. The $\text{Na}^+/\text{Sr}^{2+}$ cations were either allocated from difference Fourier maps or placed in similar sites as those in NaTEA-ZSM-25. These cations were mostly in the 8-ring sites throughout the structure. When the fractional occupancies of cations refined to values considerably greater than 1 when input as ' Na^+ ', they were instead included as more strongly scattering Sr^{2+} cations and their occupancies were refined without any restrictions. Each Na^+ or Sr^{2+} site was then modelled with a mixed occupancy with water oxygen. In this way six sites were identified as unambiguously containing Sr^{2+} cations (Sr1-Sr6). Additional scattering identified from difference Fourier mapping was included as water oxygen. The Debye-Waller factors of T, O, Na/Sr, water molecules and C(N) in the TEA^+ ions were fixed to 1, 1.5, 3, 4 and 5, respectively and all fractional atomic coordinates were refined in the final cycles. The refinement converged to $R_{wp}=0.0791$, $R_p=0.0569$ and $GOF=4.396$ (Extended Data Fig. 4a, Supplementary Table 8).

For NaTEA-PST-20, the chemical formula obtained from the elemental analysis and structure refinement was $[(\text{N}(\text{C}_2\text{H}_5)_4)_{56}\text{Na}_{560}\text{Sr}_{11}(\text{H}_2\text{O})_{586}][\text{Al}_{638}\text{Si}_{2002}\text{O}_{5280}]$; a small amount of Sr^{2+} cations still remained after the ion-exchange. Rietveld refinement was carried out in a similar way to that of as-made NaSrTEA-PST-20 and the refined unit cell was $a=55.0664(7)$ Å. The location of TEA^+ and Na^+ cations was modelled using the positions obtained from the structure model of NaTEA-ZSM-25. Additional guest water molecules were located from the difference Fourier maps by fixing the framework of NaTEA-PST-20. The Debye-Waller factors of T, O, Na/Sr, water molecules and C(N) in the TEA^+ ions were fixed to 1, 2, 3, 4 and 5, respectively and all fractional atomic coordinates refined in the final cycles. The refinement converged to $R_{wp}=0.0883$, $R_p=0.0653$ and $GOF=3.59$ (Extended Data Fig. 4b, Supplementary Table 9).

During the refinement of NaTEA-PST-20, some unindexed peaks were identified, which could be attributed to the minor impurity phases ZSM-25 and (for some smaller peaks) the even larger RHO-family member RHO-G6. Thus, the structure models of NaTEA-PST-20 and NaTEA-ZSM-25 were both included in the refinement. Considering the complexity of the two structures and the number of parameters, only the TCHZ peak profile function, zero-shift, the background with a 17th order Chebychev polynomial, and the unit cells of the two structures were refined. The atomic positions and thermal parameters were fixed based on the two structure models. The refinement was improved and converged to $R_{wp}=0.0793$, $R_p=0.0593$ and $GOF=3.16$ (Supplementary Fig. 8, Supplementary Table 9), with 92.5 wt% of PST-20 and 7.5 wt% of ZSM-25 in the sample.

The synchrotron PXRD pattern of the sample from Run 18 (Supplementary Table 3 and Supplementary Fig. 9a) was compared to those calculated based on the structure models of PST-20 and the hypothetical RHO-G6, which indicated that the sample is a mixture of RHO-G6 (denoted PST-25) and PST-20, with ca 75% PST-25. The two-phase LeBail refinement based on PST-25 and PST-20 resulted in a good agreement between the observed and the calculated profiles (Supplementary Fig. 9b; $R_{wp}=0.0221$, $R_p=0.0142$), and the unit cell parameters $a=55.0270(5)$ Å for PST-20 and $a=65.0436(4)$ Å for PST-25.

Prediction of ZSM-25 from PAU based on strong reflections. Inspired by the successful structure solution of ZSM-25 by phasing the RED data using the related PAU structure, we investigated the possibility of deducing the structure of ZSM-25 solely from the PAU structure. We compared the structure factors calculated from the frameworks of PAU and ZSM-25, and found that the intensity distribution of reflections is similar and the phases of the strong reflections are the same, as shown in Fig. 3a and Extended Data Fig. 3. We selected the 133 strongest symmetry-independent reflections of PAU with normalised structure factor $E>1.2$ and $d>1.00$ Å to predict the structure of ZSM-25 (Supplementary Table 15). The structure factor amplitudes and phases of these strong reflections were transposed to be those of a ‘hypothetical’ ZSM-25 by converting the reflection indices according to $h_{ZSM-25}=h_{PAU}\times a_{ZSM-25}/a_{PAU}$, $k_{ZSM-25}=k_{PAU}\times a_{ZSM-25}/a_{PAU}$, $l_{ZSM-25}=l_{PAU}\times a_{ZSM-25}/a_{PAU}$ and taking the nearest integers. A 3D electron density map was calculated (Extended Data Fig. 5d) and all 16 T-atoms and 31 out of 40 oxygen atoms in the asymmetric unit were located. A complete ZSM-25 framework could be obtained by adding the nine missing oxygen atoms geometrically between the T-atoms (Extended Data Fig. 5e). Compared to the 3D electrostatic potential map obtained from RED (Fig. 2e), the 3D electron density map deduced from PAU

(Extended Data Fig. 5d) has higher resolution so that most of the oxygen atoms could be resolved from the density map. This showed that the framework structure of ZSM-25 could be predicted solely from the related **PAU** framework, without using any ZSM-25 experimental diffraction data.

Prediction of new structures in the RHO-family. The structure of RHO-G2 (Extended Data Fig. 5b) ($a \approx 25 \text{ \AA}$) was predicted previously^{26,27}. The prediction of larger structures, for example RHO-G5 ($a \approx 55 \text{ \AA}$), RHO-G6 ($a \approx 65 \text{ \AA}$) etc., is very challenging. Although we know the unit cell and space group and partial structures (the cubic scaffolds) of RHO-G5 and RHO-G6, it is difficult to fill the remaining empty space between the cubic scaffolds by model building to complete these two structure models manually. We therefore used the strong reflections method we developed above to predict the structure model of RHO-G5 from RHO-G4, and the structure model of RHO-G6 from RHO-G5. Structure factor amplitudes and phases were calculated from the idealised structure model of RHO-G4 (ZSM-25). 470 strongest reflections with E -value > 1.2 and $d > 1.00 \text{ \AA}$ were selected (Supplementary Table 16). The indices of each strong reflection of RHO-G5 were calculated from the indices of the corresponding reflection of RHO-G4 according to $h_{\text{RHO-G5}} = h_{\text{RHO-G4}} \times a_{\text{RHO-G5}} / a_{\text{RHO-G4}}$, $k_{\text{RHO-G5}} = k_{\text{RHO-G4}} \times a_{\text{RHO-G5}} / a_{\text{RHO-G4}}$, $l_{\text{RHO-G5}} = l_{\text{RHO-G4}} \times a_{\text{RHO-G5}} / a_{\text{RHO-G4}}$. The 3D electron density map was calculated by inverse Fourier transformation from the amplitudes and phases adopted from those of RHO-G4 using the SUPERFLIP software³⁶ (Extended Data Fig. 5f). All 29 T-atoms and 44 out of 70 oxygen atoms in the asymmetric unit of RHO-G5 were located from the 3D map by using the EDMA software³⁷, and the remaining 26 oxygen atoms were added geometrically between the T-atoms to complete the four-connected framework (Extended Data Fig. 5g). A similar approach was applied to generate the RHO-G6 structure based on the RHO-G5 structure. The 3D electron density map (Extended Data Fig. 5h) was calculated using the 742 strongest reflections with E -value > 1.2 and $d > 1.00 \text{ \AA}$ from the RHO-G5 structure, as given in Supplementary Table 17. The calculation of indices of RHO-G6 follows the previous rules, $h_{\text{RHO-G6}} = h_{\text{RHO-G5}} \times a_{\text{RHO-G6}} / a_{\text{RHO-G5}}$, $k_{\text{RHO-G6}} = k_{\text{RHO-G5}} \times a_{\text{RHO-G6}} / a_{\text{RHO-G5}}$, and $l_{\text{RHO-G6}} = l_{\text{RHO-G5}} \times a_{\text{RHO-G6}} / a_{\text{RHO-G5}}$. All 47 T-atoms and 96 out of 112 oxygen atoms of RHO-G6 in the asymmetric unit were located from the 3D map, and the remaining 16 oxygen atoms were added geometrically between the T-atoms to complete the four-connected framework (Extended Data Fig. 5i). All the structures in the RHO-family were further energy-minimised in the pure SiO_2 forms using GULP (Supplementary Fig. 2, Supplementary Table 12), and are all energetically feasible. The corresponding unit cell parameters from RHO-G1 to RHO-G6 are 14.77, 24.58, 34.40, 44.22, 54.07 and 63.87 \AA , respectively. The energy

difference from quartz was as predicted, based on the results of earlier studies using GULP that show a clear trend between energy and framework density⁴¹. The lattice energies for the RHO-family are comparable with those for other zeolite structures built from 4- and 6-rings only, for example **SOD**, **LTA**, **FAU**, **MER**, **FAU**, **KFI**, **CHA**, **PHI**. This indicates that all structures in the RHO-family are energetically reasonable.

Gas adsorption experiments. The CO₂, CH₄, and N₂ adsorption isotherms of NaTEA-ZSM-25 and NaTEA-PST-20 were measured at 298 K and at pressures up to 1.2 bar using a Mirae SI nanoPorosity-XG analyser (Fig. 4a,b). Prior to the experiments, each zeolite sample was evacuated for 6 h at 523 K. Adsorption kinetics and adsorption-desorption cycling of CO₂ were performed using a Setaram PCTPro E&E analyzer. Prior to the experiments, the zeolite sample was evacuated for 6h at 473 K. While kinetics of CO₂ adsorption was carried out at 298 K and 1.2 bar (Fig. 4c), cyclic CO₂ adsorption was repeated 100 times at 343 K and 1.2 bar in vacuum swing regeneration mode (Fig. 4a,b).

References

31. Totktarev, A., Harris, T., Kibby, C., Ione, K. & O'Rear, D. *Proc. 12th Int. Zeolite Conf.* **1**, 2023-2030 (Materials Research Society, Warrendale, USA, 1999).
32. Chatelain T. *et al.* Synthesis and characterization of high-silica zeolite RHO prepared in the presence of 18-crown-6 ether as organic template. *Microporous Mater.* **4**, 231-238 (1995).
33. Coe, C. G., Gaffney, T. R. & Srinivasan, R. S. Chabazite for gas separation. US Patent 4, 925, 460 (1990).
34. Sheldrick, G. M. A short history of SHELX. *Acta Crystallogr.* **A64**, 112-122 (2007).
35. Gordon, E. K., Samson, S. & Kamb, W. B. Crystal structure of the zeolite paulingite. *Science* **154**, 1431-1431 (1966).
36. Palatinus, L. & Chapuis, G. SUPERFLIP-a computer program for the solution of crystal structures by charge flipping in arbitrary dimensions. *J. Appl. Crystallogr.* **40**, 786-790 (2007).
37. Palatinus, L., Prathapa, S. J. & Smaalen, S. van. EDMA: a computer program for topological analysis of discrete electron densities. *J. Appl. Crystallogr.* **45**, 575-580 (2012).
38. Young, R. A. *The Rietveld Method* (Oxford University Press,1995).

39. Le Bail, A., Duroy, H. & Fourquet, J. L. Ab-initio structure determination of LiSbWO_6 by X-ray powder diffraction. *Mater. Res. Bull.* **23**, 447–452 (1988).
40. Larson, A. C. & Von Dreele, R. B. General Structure Analysis System (GSAS), Los Alamos National Laboratory Report LAUR 86-748, (2004).
41. Henson, N. J., Cheetham, A. K. & Gale, J. D. Theoretical calculations on silica frameworks and their correlation with experiment. *Chem. Mater.* **6**, 1647-1650 (1994).

Captions for Extended Data Files

Extended Data Figure 1 | Characterization of ZSM-25 and PST-20 zeolites. Powder XRD patterns (left), ^{27}Al (middle) and ^{29}Si (right) MAS NMR spectra of as-made (bottom) and calcined (top) ZSM-25 (**a**) and PST-20 (**b**).

Extended Data Figure 2 | Reconstructed 3D reciprocal lattice from the RED data. **a-c**, NaTEA-ZSM-25 and **d-f**, NaSrTEA-PST-20. **a, c**, The 3D reciprocal lattice with the crystal inserted. **b, c, e, f**, 2D slices cut from the reconstructed 3D reciprocal lattice showing the $(h\ k\ 0)$ plane (**b, e**), $(h\ k\ h)$ (**c**) and $(h\ k\ -k)$ (**f**) reciprocal plane. The distribution of the strong reflections for NaTEA-ZSM-25 and NaSrTEA-PST-20 is similar to that of PAU.

Extended Data Figure 3 | Structure factor amplitudes and phases calculated from the structure models of RHO-G1 to RHO-G6. The $(h\ k\ -h-k)$ reflections are shown. Reflections in red have phases 0° , while those in blue have phases 180° . The red, green, and blue circles correspond to 1.0, 1.6 and $3.0\ \text{\AA}$. The frameworks are idealized in the pure SiO_2 forms.

Extended Data Figure 4 | PXRD profiles for the Rietveld refinement of as-made and Na^+ -exchanged NaSrTEA-PST-20. **a**, As-made NaSrTEA-PST-20. **b**, Na^+ -exchanged NaSrTEA-PST-20 (denoted NaTEA-PST-20). The observed, calculated and difference curves are in blue, red and black, respectively. The good agreement of observed and calculated data at high-angles (inset) indicates that the framework structure is correct. The slight differences at lower angles are due to incomplete determination of the positions of all guest molecules/cations ($\lambda = 0.40091\ \text{\AA}$).

Extended Data Figure 5 | The prediction of the RHO-family members RHO-G1-G6 from the structure of PAU (RHO-G3). The arrows indicate how the structures were predicted from their nearest generations. The 3D electron density map of RHO-Gn ($n = 4-6$) was

generated using the structure factors of strong reflections from RHO-*Gn*-1, and a 3D structure model of RHO-*Gn* could be built. The structures of RHO-G1 and RHO-G2 could be obtained from RHO-G3 by model building.

Extended Data Figure 6 | Tile representations of the structures of RHO-G1-G6 in the RHO-family. The structure expansion operates at two levels: first, isorecticular expansion of the scaffold by inserting a pair of *pau* and *d8r* cages along each unit cell edge (top); second, embedding of other cages (middle) in the inter-scaffold space. The resulting frameworks are denoted as *embedded isorecticular zeolite structures* (bottom).

Extended Data Table 1 | Structure factor amplitudes of the strongest reflections obtained from RED data, and the corresponding reflections and structure factor phases in the PAU structure. The amplitudes $|F_{\text{ZSM-25}}|$ were calculated as the square-roots of the intensities extracted from RED. The indices of the corresponding reflections in the PAU structure were obtained: $h_{\text{PAU}} = h_{\text{ZSM-25}} \times a_{\text{PAU}}/a_{\text{ZSM-25}}$, $k_{\text{PAU}} = k_{\text{ZSM-25}} \times a_{\text{PAU}}/a_{\text{ZSM-25}}$, $l_{\text{PAU}} = l_{\text{ZSM-25}} \times a_{\text{PAU}}/a_{\text{ZSM-25}}$, where the unit cell $a_{\text{PAU}} = 35 \text{ \AA}$ and $a_{\text{ZSM-25}} = 45 \text{ \AA}$.

Extended Data Table 2 | Room-temperature CO₂/CH₄ and CO₂/N₂ selectivities at 0.1 and 1.0 bar for NaTEA-PST-20, NaTEA-ZSM-25, NaTEA-ECR-18, Na-Rho, and K-chabazite. The CO₂/CH₄ and CO₂/N₂ selectivities are defined as $(Q_{\text{CO}_2})/(Q_{\text{CH}_4})$ and $(Q_{\text{CO}_2})/(Q_{\text{N}_2})$, respectively, where Q_{CO_2} , Q_{CH_4} , and Q_{N_2} are the equilibrium molar uptakes of CO₂, CH₄, and N₂ at a given pressure taken from the corresponding single component isotherms, respectively.